

First-principles prediction of phase transformation and mechanical properties of Mn_2AlB_2 under high pressure

Yi-Xian Wang(王乙先), Zhe Yuan(袁喆), Wu-Na Xie(谢武娜), Yi-Yang Qiu(邱一洋), and Zhao-Qi Wang(王朝棋)
Citation: Chin. Phys. B, 2026, 35 (**7**): 076105. DOI: 10.1088/1674-1056/ae3134
http://cpb.iphy.ac.cn; http://iopscience.iop.org/cpb

What follows is a list of articles you may be interested in

High-pressure synthesis, crystal structure, and electronic properties of $Ba_9Zr_{2.79}Te_{15}$

Runteng Chen(陈润滕), Guodong Wang(王国东), Zhe Wang(王哲), Wenmin Li(李文敏), Jianfa Zhao(赵建发), Zheng Deng(邓正), Heng Wang(王恒), Xiancheng Wang(望贤成), Jun Zhang(张俊), and Changqing Jin(靳常青)
Chin. Phys. B, 2026, 35 (**6**): 066101. DOI: 10.1088/1674-1056/ae521a

Physical properties of Cr_2S_3 at high pressure

Lun Xiong(熊伦), Mingquan Jiang(江明全), Jinxia Zhu(竹锦霞), Lin Xia(夏林), Hao Wang(王毫), Shenghan Zhang(张升瀚), Pengfei Tang(汤鹏飞), Zhiqiang Chen(陈志强), Sheng Jiang(蒋升), and Hongliang Dong(董洪亮)
Chin. Phys. B, 2026, 35 (**3**): 036103. DOI: 10.1088/1674-1056/ae1cb3

Pressure-induced phase transition in transition metal trifluorides

Peng Liu(刘鹏), Meiling Xu(徐美玲), Jian Lv(吕健), Pengyue Gao(高朋越), Chengxi Huang(黄呈熙), Yinwei Li(李印威), Jianyun Wang(王建云), Yanchao Wang(王彦超), and Mi Zhou(周密)
Chin. Phys. B, 2022, 31 (**10**): 106104. DOI: 10.1088/1674-1056/ac5887

Prediction of scandium tetraboride from first-principles calculations: Crystal structures, phase stability, mechanical properties,and hardness

Bin-Hua Chu(初斌华) and Yuan Zhao(赵元)
Chin. Phys. B, 2021, 30 (**7**): 076107. DOI: 10.1088/1674-1056/abe116

Geoscience material structures prediction via CALYPSO methodology

Andreas Hermann
Chin. Phys. B, 2019, 28 (**10**): 106107. DOI: 10.1088/1674-1056/ab43bc

---

First-principles prediction of phase transformation and mechanical properties of Mn_2AlB_2 under high pressure

Yi-Xian Wang(王乙先)[1,†], Zhe Yuan(袁喆)[1], Wu-Na Xie(谢武娜)[2], Yi-Yang Qiu(邱一洋)[1], and Zhao-Qi Wang(王朝棋)[1,‡]

[1] *College of Science, Xi'an University of Science and Technology, Xi'an* 710054, *China*

[2] *Henan Joint International Research Laboratory of New Energy Materials and Devices, School of Physics and Electronics, Henan University, Kaifeng* 475004, *China*

(Received 12 November 2025; revised manuscript received 22 December 2025; accepted manuscript online 26 December 2025)

We employ the particle swarm optimization (PSO) algorithm in combination with first-principles calculations to systematically investigate the phase stability and physical properties of Mn_2AlB_2 under pressures of up to 80 GPa. The results reveal a pressure-induced phase transition from orthorhombic *oC*10-Mn_2AlB_2 to tetragonal *tP*10-Mn_2AlB_2 at approximately 21.5 GPa, accompanied by a volume collapse of approximately 1.6%, confirming a first-order phase transition. Both phases are mechanically and dynamically stable, with the bulk and shear moduli increasing under compression. The *B*/*G* ratio and Poisson's ratio indicate a pressure-driven brittle-to-ductile transition occurs at pressures above 50 GPa. The calculated Vickers hardness suggests that the two Mn_2AlB_2 phases are potential hard materials rather than superhard ones. Furthermore, the minimum thermal conductivity of both phases exceeds 1.25 $W\cdot m^{-1}\cdot K^{-1}$, and they are not suitable as thermal barrier coating materials. Electronic structure and bonding analyses reveal that pressure strengthens Mn–B and Al–B bonds and reduces magnetic moments, providing a microscopic explanation for the pressure-dependent mechanical behavior. Finally, a high-pressure and high-temperature phase diagram of Mn_2AlB_2 is constructed for the first time using the quasi-harmonic approximation (QHA) method. The results show that the transformation pressure from *oC*10-Mn_2AlB_2 to *tP*10-Mn_2AlB_2 decreases with increasing temperature. These findings deepen our understanding of the pressure-induced behavior of Mn_2AlB_2 and provide theoretical guidance for its mechanical optimization and high-pressure synthesis.

Keywords: crystal structure prediction, high pressure, mechanical properties, phase transition

PACS: 61.50.Ah, 62.50.–p, 62.23.–c, 64.60.–i

DOI: 10.1088/1674-1056/ae3134 **CSTR:** 32038.14.CPB.ae3134

1. Introduction

Nanolaminate materials are promising candidates for future energy, transportation, and defense applications due to their exceptional mechanical, electrical, and magnetic properties, as well as their superior radiation tolerance.[1–3] The most representative nanolaminate materials are the MAX phases, expressed by the general formula $M_{n+1}AX_n$ (n = 1, 2, or 3),[4] where M represents a transition metal, A denotes an A-group element, typically referring to elements from groups 13–16, and X is carbon or nitrogen. These materials consist of strongly bonded M–X layers that alternate with relatively weakly bonded A layers.[5] Owing to their unique layered bonding structure, MAX phases exhibit high thermal and mechanical stability, excellent electrical and thermal conductivity, and notable hardness and stiffness, thereby earning the designation 'metallic ceramics'.[6–8] However, the alternation of strongly bonded M–X layers and weakly bonded A layers limits their fracture toughness and damage tolerance, motivating the exploration of alternative layered architectures.[2,9,10] One effective approach involves inserting main-group elements into binary boride lattices to form weakly bonded interfaces,[11–14] resulting in ternary metal borides known as MAB phases. In 2015, Ade and Hillebrecht first discovered through experiments that MAB compounds exhibit a nanolaminate structure analogous to that of MAX phases.[15]

Among the various MAB phases, Mn_2AlB_2 has been extensively studied under ambient conditions. In 2018, Kota *et al.*[16] successfully synthesized dense single-phase Mn_2AlB_2 by reactive hot pressing and reported that its Young's modulus and shear modulus at 300 K were 243 GPa and 102 GPa, respectively. Subsequently, Potashnikov *et al.*[17] further revealed that Mn_2AlB_2 exhibits canted antiferromagnetism below 390 K. Later, Gokhan *et al.*[18] performed a comprehensive theoretical study of the structural, electronic, magnetic, elastic, and lattice dynamical properties of M_2AlB_2 (M = Mn, Fe, Co), confirming its thermodynamic, mechanical, and dynamical stability. In 2021, Liu *et al.*[19] further demonstrated the metallic behavior and covalent M–B bonding of Mn_2AlB_2 by combining the quasi-harmonic Debye model with density functional theory. More recently, Kota *et al.*[20] reported the thermoelectric properties of Mn_2AlB_2, revealing nearly isotropic thermoelectric behavior.

Despite these efforts, previous research has primarily focused on ambient pressure, leaving the high-pressure struc-

†Corresponding author. E-mail: lsdwyx@163.com

‡Corresponding author. E-mail: zhqwangsc@foxmail.com

© 2026 Chinese Physical Society and IOP Publishing Ltd. All rights, including for text and data mining, AI training, and similar technologies, are reserved.

tural evolution and potential phase transitions of Mn_2AlB_2 largely unexplored. High pressure can significantly alter the crystal structure, electronic structure, and mechanical properties of materials, which is critical for understanding their stability and potential applications. In this work, we employ the particle swarm optimization (PSO) algorithm to systematically investigate the crystal structure of Mn_2AlB_2 over a wide pressure range (0–80 GPa). Subsequently, we construct a temperature–pressure phase diagram for Mn_2AlB_2 using the quasi-harmonic approximation method and determine the finite-temperature phase boundaries. We further present a detailed analysis of the mechanical properties and minimum thermal conductivity of different Mn_2AlB_2 phases. These results are expected to offer theoretical guidance for the experimental synthesis and property optimization of Mn_2AlB_2 under high pressure while enhancing our understanding of the high-pressure behavior of ternary layered MAB phases.

2. Computational details

Using the CALYPSO[21,22] code with a variable-well PSO algorithm, crystal structure prediction is performed for the pressure range of 0–80 GPa using up to four formula units (FUs) per simulation cell. The PSO algorithm, which only needs the chemical compositions of a compound at given pressures, can search for crystal structures with the lowest enthalpy and has been successfully applied to many materials.[23–25] All structural optimizations are implemented in the Vienna *Ab initio* Simulation Package (VASP).[26,27] The computational outputs from VASP are refined using the VASPKIT tool.[28] The ion–electron interaction is described by a projector-augmented wave pseudopotential[29] method, and $3d^5 4s^2$, $3s^2 3p^1$, and $2s^2 2p^1$ are treated as the valence electrons of Mn, Al, and B, respectively. The Perdew–Burke–Ernzerhof (PBE)[30] functional is employed to describe the electronic exchange–correlation interactions. A cutoff energy of 600 eV and a Monkhorst–Pack k-point mesh spacing of $2\pi \times 0.03$ Å^{-1} are used to ensure good convergence of the total enthalpy values. The convergence criteria for the total energy and maximum force in structural relaxation are 1×10^{-8} eV/atom and 0.01 eV/Å, respectively. In addition, the bulk modulus B and shear modulus G are estimated using the Voigt–Reuss–Hill approximation.[31–34] Phonon dispersion calculations are performed using the finite displacement method in the PHONOPY code.[35,36] A $2 \times 2 \times 2$ supercell (containing 80 atoms) is used to ensure the convergence of phonon frequencies. Correlation effects among the Mn 3d electrons are treated using the GGA + U approach,[37] adopting the Coulomb interaction $U = 0.6$ eV applied to Mn atoms, while no U correction is imposed on Al or B. Furthermore, we calculate the band-resolved projected crystal orbital Hamilton populations (COHPs) for chemical bonding analysis, which is performed using the Local Orbital Basis Suite Towards Electronic-Structure Reconstruction (LOBSTER) package.[38,39]

3. Results and discussion

3.1. Structural properties

Our simulations indicate that $oC10$-Mn_2AlB_2 (Fig. 1(a)) is the most stable structure at zero pressure, which is in agreement with previous theoretical[18,19] and experimental[13] studies, thus validating the reliability of our computational approach. At 30 GPa, the tetragonal $tP10$-Mn_2AlB_2 (Fig. 1(b)) exhibits the lowest enthalpy. Before evaluating the pressure-induced phase stability, we compared the formation enthalpies of different magnetic states. The results indicate that the ferromagnetic (FM) configuration (−0.20 eV/atom) consistently possesses a lower formation enthalpy than the antiferromagnetic (AFM) configuration (−0.19 eV/atom) throughout the examined pressure range, confirming that FM is the magnetic ground state of Mn_2AlB_2. Therefore, the following discussions focus on the FM state. The predicted lattice parameters and atomic coordinates of $oC10$-Mn_2AlB_2, $oI10$-Mn_2AlB_2, and $tP10$-Mn_2AlB_2 under pressure are summarized in Table 1. Additionally, the formation enthalpy was calculated using the equation $\Delta H = H(Mn_2AlB_2) - 2H(Mn) - H(Al) - 2H(B)$, where the reference structures are Mn in the α phase, Al in a face-centered cubic structure, and boron in the α phase (below 20 GPa) or γ boron (above 20 GPa), respectively. As shown in Table 1, $oC10$-Mn_2AlB_2 exhibits the lowest formation enthalpy (−0.20 eV/atom) at 0 GPa, indicating that it is the most stable phase at 0 K and zero pressure, consistent with previous theoretical results. Furthermore, the calculated formation enthalpies of $oI10$-Mn_2AlB_2 and $tP10$-Mn_2AlB_2 are 0.09 eV/atom and −0.17 eV/atom, respectively, suggesting that $oI10$-Mn_2AlB_2 may decompose into other stable structures at 0 K and zero pressure, whereas $tP10$-Mn_2AlB_2 could potentially exist as a metastable phase under these conditions.

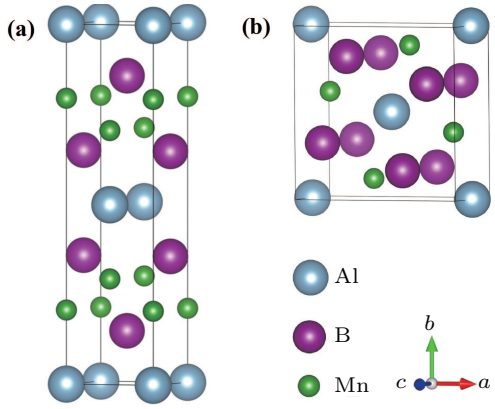


Fig. 1. Crystal structures of (a) $oC10$-Mn_2AlB_2 at 0 GPa, (b) $tP10$-Mn_2AlB_2 at 30 GPa. The light blue, purple, and green spheres represent Al, Mn, and B atoms, respectively.

Table 1. Predicted lattice constants, atomic positions, and formation enthalpies (in eV·atom^{-1}) of $oC10$-Mn_2AlB_2, $oI10$-Mn_2AlB_2, and $tP10$-Mn_2AlB_2 at different pressures, together with the available experimental and theoretical data.

Space group	Pearson symbol	Parameters (Å)	Atom	x	y	z	ΔH	Ref.
Cmmm	*oC*10	$a = 2.893$	Mn(4*j*)	0.000	0.354	0.500	−0.20	This work
(0 GPa)		$b = 11.094$	Al(2*a*)	0.000	0.000	0.000		
		$c = 2.833$	B(4*i*)	0.000	0.206	0.000		
	*oC*10	$a = 2.923$	Mn(4*j*)	0.000	0.356	0.500		Exp.[13]
		$b = 11.071$	Al(2*a*)	0.000	0.000	0.000		
		$c = 2.900$	B(4*i*)	0.000	0.201	0.000		
	*oC*10	$a = 2.894$						Cal.[18]
		$b = 11.070$						
		$c = 2.828$						
	*oC*10	a =2.905						Cal.[19]
		$b = 11.079$						
		$c = 2.841$						
Immm	*oI*10	$a = 3.242$	Mn(4*g*)	0.500	0.798	0.500	0.09	This work
(0 GPa)		$b = 6.210$	Al(2*b*)	0.000	0.500	0.500		
		$c = 4.516$	B(4*i*)	0.000	0.000	0.312		
*P*4/*mbm*	*tP*10	$a = b = 5.598$	Mn(4*g*)	0.171	0.329	0.000	−0.17	This work
(0 GPa)		$c = 2.828$	Al(2*b*)	0.500	0.500	0.500		
			B(4*h*)	0.386	0.114	0.500		
*P*4/*mbm*	*tP*10	$a = b = 5.427$	Mn(4g)	0.172	0.327	0.000	−0.41	This work
(30 GPa)		$c = 2.734$	Al(2*b*)	0.500	0.500	0.500		
			B(4*h*)	0.385	0.114	0.500		
*P*4/*mbm*	*tP*10	$a = b = 5.239$	Mn(4*g*)	0.173	0.326	0.000	−0.67	This work
(80 GPa)		$c = 2.636$	Al(2*b*)	0.500	0.500	0.500		
			B(4*h*)	0.384	0.116	0.500		

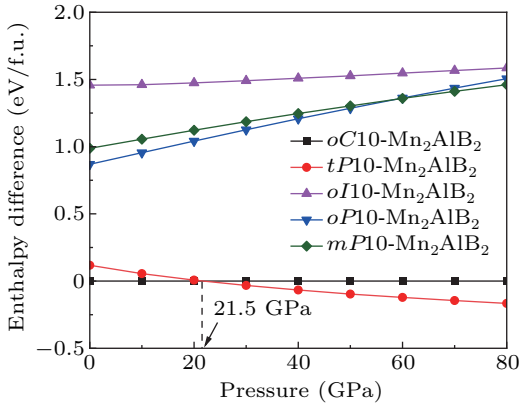


Fig. 2. Calculated enthalpy differences of various intermetallic phases of Mn_2AlB_2 versus pressure.

To determine the transition pressure at 0 K, the enthalpy differences of $tP10$-Mn_2AlB_2 relative to $oC10$-Mn_2AlB_2 were calculated under various pressures and plotted in Fig. 2. As shown in Fig. 2, $oC10$-Mn_2AlB_2 exhibits the lowest enthalpy at 0 K and zero pressure, confirming its stability as the ground-state structure. With increasing pressure up to 18 GPa, $tP10$-Mn_2AlB_2 gradually becomes more stable and surpasses all other phases above 21.5 GPa. Thereafter, it remains structurally stable, with no further phase transitions observed up to 80 GPa. Therefore, the pressure-induced phase transition sequence of Mn_2AlB_2 can be identified as $oC10$-Mn_2AlB_2 → $tP10$-Mn_2AlB_2.

To evaluate the dynamical stability of $oC10$-Mn_2AlB_2 and $tP10$-Mn_2AlB_2 under different pressures, their phonon dispersion curves were systematically calculated using the finite-displacement method. As shown in Fig. 3, no imaginary phonon modes are observed for $oC10$-Mn_2AlB_2 in the pressure range of 0–21.5 GPa and for $tP10$-Mn_2AlB_2 in the pressure range of 21.5–80 GPa, confirming their dynamical stability under the investigated conditions. Furthermore, by fitting the energy–volume data to the Vinet equation of state, pressure–volume curves of Mn_2AlB_2 in the range of 0–80 GPa were obtained, as shown in Fig. 4. These results indicate that the transition from $oC10$-Mn_2AlB_2 to $tP10$-Mn_2AlB_2 is accompanied by a volume reduction of approximately 1.60%, characteristic of a first-order phase transition.

3.2. Mechanical properties

Elastic constants provide critical insights into a material's ability to withstand external forces and maintain structural integrity under different conditions. The calculated elastic constants of $oC10$-Mn_2AlB_2 and $tP10$-Mn_2AlB_2 at various pressures were determined using the stress–strain method.[40] The results are listed in Table 2, and theoretical data[11,18,19] are also illustrated for comparison. Obviously, our obtained results are consistent with the other available data. Unfortunately, no other data are available for comparison with the predicted high-pressure phase $tP10$-Mn_2AlB_2. As shown in Table 2, the elastic constants C_{33} of both $oC10$-Mn_2AlB_2 and

$tP10$-Mn_2AlB_2 are consistently larger than C_{11} and C_{22}, indicating that resistance to deformation in the [001] direction is greater than that in the [100] and [010] directions. This anisotropy in elastic response suggests that the material may exhibit direction-dependent mechanical behavior under applied stress.

Table 2. Calculated elastic constants C_{ij} (in GPa) of different Mn_2AlB_2 phases at different pressures, together with the available calculated results.

Space group	Pressure (GPa)	C_{11}	C_{12}	C_{13}	C_{22}	C_{23}	C_{33}	C_{44}	C_{55}	C_{66}	Ref.
$oC10$	0	508.4	186.8	110.9	402.8	128.1	519.3	166.7	211.1	182.4	This work
	0	486.0	194.0	132.0	413.0	140.0	478.0	152.0	192.0	187.0	Cal.[11]
	0	467.5	172.4	105.1	342.8	94.8	459.7	154.7	195.9	170.4	Cal.[18]
	0	495.5	186.9	109.5	428.4	137.4	487.2	154.1	193.1	185.5	Cal.[19]
	10	537.8	204.7	125.7	456.5	146.5	555.3	181.4	225.9	196.4	This work
	21.5	609.6	242.0	160.9	538.0	181.7	629.0	205.7	257.6	220.1	This work
$tP10$	21.5	568.1	288.2	195.8			630.6	249.3		197.5	This work
	30	617.3	313.8	220.6			682.1	269.2		212.5	This work
	40	674.2	343.7	249.4			741.1	291.9		229.7	This work
	50	732.6	370.1	274.0			802.9	313.5		245.0	This work
	60	785.8	398.5	301.3			859.1	334.2		259.9	This work
	70	837.8	426.3	328.3			914.2	354.3		274.4	This work
	80	887.5	454.9	355.5			968.3	373.8		288.7	This work

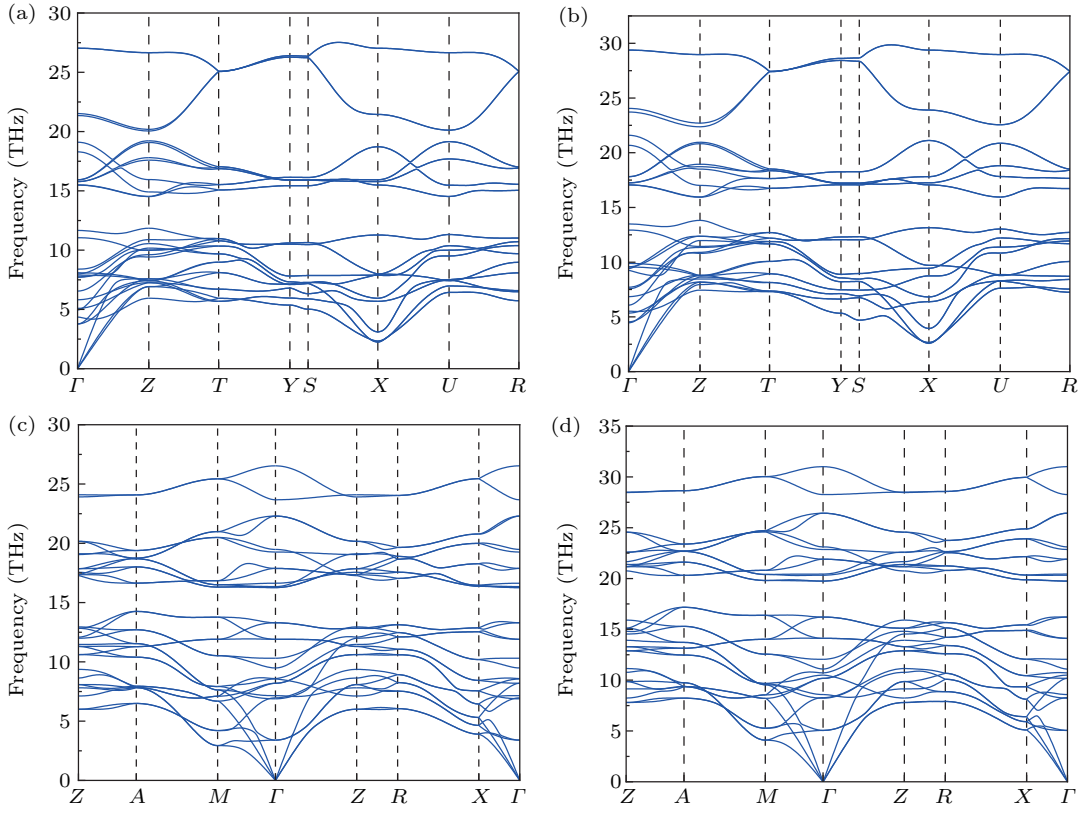


Fig. 3. Phonon dispersion curves of $oC10$-Mn_2AlB_2 at (a) 0 GPa and (b) 21.5 GPa, and $tP10$-Mn_2AlB_2 at (c) 21.5 GPa and (d) 80 GPa.

It is essential to confirm mechanical stability[41] when studying the mechanical properties of a compound. For the orthorhombic $oC10$-Mn_2AlB_2 phase, the mechanical stability criteria are

$$\begin{aligned}&\tilde{C}_{ii}>0,\ \ (i=1,2,3,4,5,6),\\&\tilde{C}_{11}+\tilde{C}_{22}+\tilde{C}_{33}+2(\tilde{C}_{12}+\tilde{C}_{13}+\tilde{C}_{23})>0,\\&\tilde{C}_{ii}+\tilde{C}_{jj}-2\tilde{C}_{ij}>0,\ \ (i,j=1,2,3,i\neq j).\end{aligned}\tag{1}$$

Similarly, the mechanical stability condition for the tetragonal $tP10$-Mn_2AlB_2 phase can be expressed as

$$\begin{aligned}&\tilde{C}_{ii}>0,\ \ (i=1,3,4,6),\\&\tilde{C}_{11}-\tilde{C}_{12}>0,\ \ \tilde{C}_{11}+\tilde{C}_{33}-2\tilde{C}_{13}>0,\\&2\left(\tilde{C}_{11}+\tilde{C}_{12}\right)+\tilde{C}_{33}+4\tilde{C}_{13}>0.\end{aligned}\tag{2}$$

It can be seen in Table 2 that $oC10$-Mn_2AlB_2 and $tP10$-Mn_2AlB_2 are mechanically stable at different pressures, as

their elastic constants meet the above mechanical stability criteria.

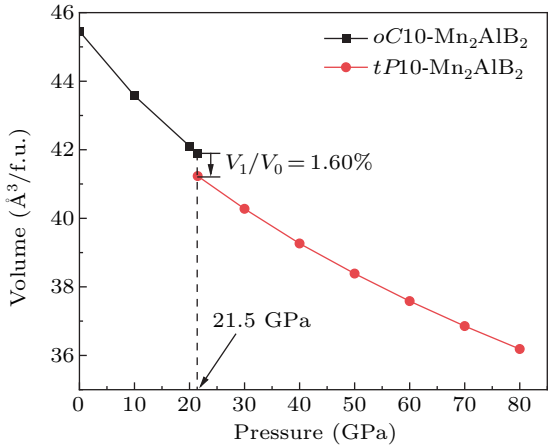


Fig. 4. Calculated volume as a function of pressure for $oC10$-Mn_2AlB_2 and $tP10$-Mn_2AlB_2, where V_0 represents the equilibrium volume of $oC10$-Mn_2AlB_2.

The calculated elastic constants were used to evaluate the bulk modulus B and shear modulus G of $oC10$-Mn_2AlB_2 and $tP10$-Mn_2AlB_2 under various pressures, based on the Voigt–Reuss–Hill approximation. In addition, Young's modulus E and Poisson's ratio υ were calculated at various pressures using the following equation:

$$E = \frac{9BG}{3B+G}, \tag{3}$$

$$\upsilon = \frac{3B-2G}{6B+2G}. \tag{4}$$

The calculated values of B, G, E, B/G, υ, and H_V for $oC10$-Mn_2AlB_2 and $tP10$-Mn_2AlB_2 are listed in Table 3 at different pressures, together with available theoretical data.[14,16,18,19] Our results for $oC10$-Mn_2AlB_2 agree with the other theoretical results at 0 GPa, further confirming the reliability of our calculations. In general, the bulk modulus serves as a primary indicator for assessing the mechanical behavior of solids, as it reflects their resistance to volumetric compression, while the shear modulus represents their ability to resist deformation induced by shear stress. As shown in Table 3, under varying pressures, both $oC10$-Mn_2AlB_2 and $tP10$-Mn_2AlB_2 exhibit stronger resistance to volumetric compression than to shear deformation. Moreover, both B and G increase with pressure, indicating the materials' enhanced resistance to compression and shear at elevated pressures. Additionally, the Young's modulus of a compound is identified as the ratio of linear stress to linear strain and thus provides useful information about its stiffness. The calculated Young's moduli for $oC10$-Mn_2AlB_2 and $tP10$-Mn_2AlB_2 are greater than 420 GPa; thus, they can be classified as relatively stiff compounds.

To evaluate the potential technological applications of Mn_2AlB_2, we analyzed its brittle or ductile behavior. According to the Pugh criterion,[42] the brittleness or ductility of a material can be determined by the ratio of its bulk modulus to its shear modulus (B/G). When this ratio exceeds the critical value of 1.75, the material exhibits ductile behavior; conversely, the material shows brittleness. As shown in Table 3, the B/G ratio of $oC10$-Mn_2AlB_2 remains less than 1.75 at pressures below the transition pressure, indicating typical brittle behavior. Above the transition pressure, $tP10$-Mn_2AlB_2 remains brittle up to 40 GPa but gradually becomes more ductile at higher pressures, as indicated by the increasing B/G ratio. Notably, although conventional MAX phases combine the advantages of metals and ceramics, their limited fracture toughness and damage tolerance remain a concern. In contrast, MAB phases achieve a better balance between structural rigidity and tunability. Our results demonstrate that external pressure can effectively enhance the ductility of Mn_2AlB_2, significantly improving its mechanical performance and expanding its potential for practical applications under extreme conditions. Furthermore, its Poisson's ratio[43] exhibits a trend consistent with the B/G ratio. For $oC10$-Mn_2AlB_2, it remains below 0.26 before the transition pressure is reached, confirming brittle behavior. The Poisson's ratio of $tP10$-Mn_2AlB_2 remains less than 0.26 between the transition pressure and 40 GPa and gradually increases above 50 GPa. This trend suggests a gradual enhancement of ductility at higher pressures, which will be further discussed in terms of the underlying bonding and electronic structure.

Hardness is a critical elastic property that determines the wear resistance of materials;[44] therefore, we employ the empirical model,[45] which has been successfully applied to a wide range of material systems,[46–49] to estimate the hardness of these compounds in this work. This model is expressed as

$$H_V = 2\left(k^2G\right)^{0.585} - 3; \quad k = G/B. \tag{5}$$

As summarized in Table 3, the calculated Vickers hardness of $oC10$-Mn_2AlB_2 at 0 GPa is 23.28 GPa, which agrees well with previous theoretical predictions.[19] Moreover, we can observe that the Vickers hardness of the two Mn_2AlB_2 phases gradually increases as the pressure increases. This trend indicates that lattice compression under pressure shortens covalent bond lengths and strengthens interatomic bonding, thereby enhancing hardness. The Vickers hardness of both phases remains below 40 GPa, suggesting that they are potential hard materials rather than superhard ones.

Since the anisotropy of elastic constants can lead to directionally dependent mechanical properties, fully characterizing such anisotropic behavior is crucial for understanding the mechanical responses of materials. To provide a comprehensive and intuitive assessment of elastic anisotropy, three-dimensional (3D) surfaces were constructed based on the directional dependence of the inverse elastic moduli.[50] The minimum bulk modulus B_{min}, maximum bulk modulus B_{max},

and their corresponding 3D surface representations under different pressures are shown in Fig. 5(a). For the $oC10$-Mn_2AlB_2 phase, within the pressure range of 0–21.5 GPa, the anisotropy along the (100) and (010) planes gradually decreases, while the (001) plane exhibits nearly isotropic behavior. Overall, the degree of anisotropy decreases with increasing pressure. In contrast, the anisotropy of the three crystallographic planes in the high-pressure phase $tP10$-Mn_2AlB_2 gradually diminishes with increasing pressure. Meanwhile, both B_{min} and B_{max} increase with pressure, and their difference remains nearly constant, indicating that pressure exerts only a limited influence on the anisotropy of the bulk modulus. This trend is clearly reflected in the pressure-induced evolution of the 3D surfaces.

Table 3. Calculated bulk moduli B (in GPa), shear moduli G (in GPa), Young's moduli E (in GPa), B/G, Poisson's ratios υ, and Vickers hardnesses H_V (in GPa) of different Mn_2AlB_2 phases at different pressures, together with the available calculated results.

Space group	Pressure (GPa)	B	G	E	B/G	υ	H_V	Ref.
$oC10$	0	252.8	176.1	428.7	1.44	0.217	23.28	This work
	0	226.0	161.0	390.0	1.40			Cal.[14]
	0	221.6	160.6	388.0	1.40			Cal.[18]
	0	252.9	169.7	394.5	1.49		22.23	Cal.[19]
	0	131.0	102.0	243.0				Exp.[16]
	10	277.8	189.6	463.5	1.46	0.222	23.89	This work
	21.5	327.1	213.5	526.0	1.53	0.232	24.39	This work
$tP10$	21.5	347.4	206.9	518.0	1.68	0.251	20.72	This work
	30	380.7	222.7	559.0	1.71	0.255	21.25	This work
	40	419.3	240.5	605.8	1.74	0.259	21.82	This work
	50	456.0	259.1	653.5	1.76	0.261	22.70	This work
	60	492.5	275.4	696.4	1.79	0.264	23.15	This work
	70	528.4	291.2	738.0	1.81	0.267	23.57	This work
	80	563.9	306.2	777.8	1.84	0.270	23.88	This work

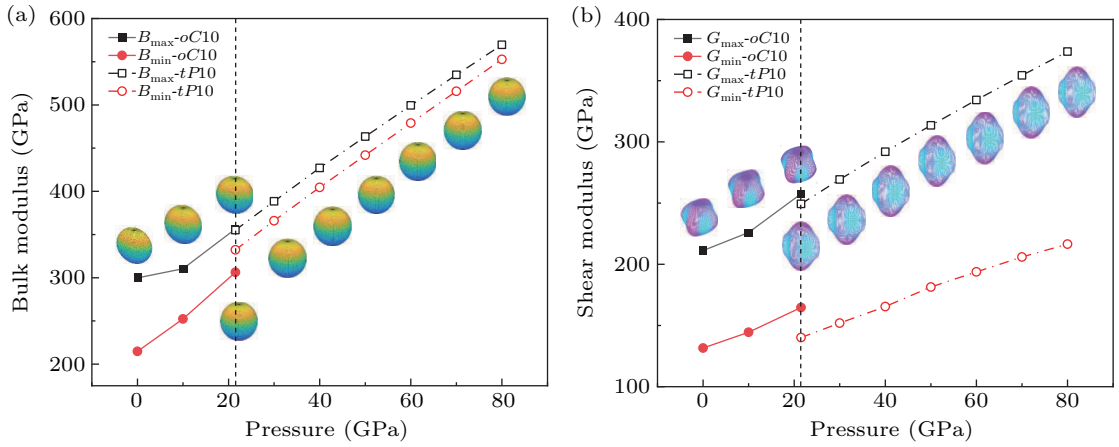


Fig. 5. Pressure-induced changes in elastic modulus and corresponding three-dimensional surface structures of $oC10$-Mn_2AlB_2 and $tP10$-Mn_2AlB_2: (a) bulk modulus B and (b) shear modulus G. The dashed vertical line indicates the phase transition pressure.

The minimum shear modulus G_{min}, maximum shear modulus G_{max}, and their pressure-dependent 3D surface representations are shown in Fig. 5(b). Both G_{min} and G_{max} increase with rising pressure, and the large difference between them indicates a pronounced shear anisotropy, which is clearly reflected in the pressure-induced evolution of the 3D surfaces. Specifically, for the $oC10$-Mn_2AlB_2 phase within the pressure range of 0–21.5 GPa, the (100) plane exhibits nearly isotropic behavior, whereas the (010) and (001) planes display significant anisotropy, with that of the (010) plane continuously strengthening under compression. In the $tP10$-Mn_2AlB_2 phase, all three crystallographic planes exhibit pronounced anisotropy. Among them, the anisotropy along the (100) and (010) planes increases with increasing pressure, while the anisotropy along the (001) plane shows exactly the opposite trend.

3.3. Debye temperature and minimum thermal conductivity

As a fundamental parameter of the thermodynamic properties of materials, the Debye temperature Θ is related to specific heat, thermal expansion, and elastic constants. It can be estimated using the following equation:[51]

$$\Theta = \frac{h}{k_B}\left[\frac{3n}{4\pi}\left(\frac{N_A\rho}{M}\right)\right]^{\frac{1}{3}} v_m, \tag{6}$$

where h is Planck's constant, k_B is Boltzmann's constant, n is the number of atoms per formula unit, N_A is Avogadro's number, M is the molar mass, ρ is the density, and v_m is the average sound velocity, which can be estimated using Navier's equation. Then, the Grüneisen parameter γ can be calculated as follows:

$$\gamma = \frac{3}{2}\left(\frac{1+\upsilon}{2-3\upsilon}\right). \tag{7}$$

The calculated values of v_t, v_l, v_m, Θ, and γ for different Mn_2AlB_2 phases at various pressures are listed in Table 4, along with the available theoretical data.[19] These calculations allow us to assess how pressure influences the elastic response, Debye temperature, and lattice anharmonicity, which are closely related to the material's hardness and thermal behavior. At zero pressure, the Debye temperature of $oC10$-Mn_2AlB_2 is approximately 867 K, in good agreement with previously reported values.[19] For the high-pressure $tP10$-Mn_2AlB_2 phase, the Debye temperature reaches about 932 K at 21.5 GPa. As pressure increases, the Θ values of the two phases exhibit a consistent rising trend. This can be attributed to the fact that lattice compression raises the atomic vibration frequency and the average sound velocity, thereby increasing the Θ value. In general, the Debye temperature is closely correlated with the microhardness of the material. The higher the Θ value, the greater the microhardness. Therefore, applying pressure can effectively enhance the microscopic hardness of both $oC10$-Mn_2AlB_2 and $tP10$-Mn_2AlB_2. Furthermore, γ provides insight into the anharmonicity of a crystal lattice, with larger values reflecting stronger anharmonic effects. At 21.5 GPa, the Grüneisen parameter γ of $oC10$-Mn_2AlB_2 is lower than that of $tP10$-Mn_2AlB_2, indicating that $tP10$-Mn_2AlB_2 exhibits stronger anharmonicity and potentially higher lattice vibrational contributions to its thermodynamic properties. Moreover, γ gradually increases with rising pressure for both phases.

Table 4. Densities ρ (in g/cm^3), transverse sound velocities v_t (in km/s), longitudinal sound velocities v_l (in km/s), average sound velocities v_m (in km/s), Debye temperatures Θ (in K), and Grüneisen parameters γ of different Mn_2AlB_2 phases at different pressures.

Space group	Pressure (GPa)	ρ	v_t	v_l	v_m	Θ	γ	Ref.
$oC10$	0	5.789	5.459	9.083	6.038	867.428	1.355	This work
	0	5.76	5.43	9.12	6.01	854.68		Cal.[19]
	10	6.039	5.604	9.374	6.201	897.311	1.374	This work
	21.5	6.281	5.830	9.869	6.459	946.905	1.417	This work
$tP10$	21.5	6.382	5.694	9.882	6.323	931.940	1.507	This work
	30	6.534	5.838	10.183	6.485	963.317	1.525	This work
	40	6.702	5.991	10.508	6.658	997.508	1.545	This work
	50	6.855	6.148	10.812	6.834	1031.597	1.555	This work
	60	7.001	6.272	11.081	6.975	1060.210	1.571	This work
	70	7.140	6.386	11.330	7.104	1087.032	1.586	This work
	80	7.272	6.488	11.561	7.221	1111.603	1.601	This work

The minimum thermal conductivity is a key parameter for evaluating materials in high-temperature applications, as thermal conductivity generally decreases with increasing temperature until it approaches a limiting value, known as the minimum thermal conductivity.[52,53] Investigating the minimum thermal conductivity helps us understand the high-temperature performance of different Mn_2AlB_2 phases and broadens their potential applications in various fields. In this study, two theoretical models proposed by Clarke[54,55] and Cahill[56] are employed to estimate the minimum thermal conductivities of $oC10$-Mn_2AlB_2 and $tP10$-Mn_2AlB_2 under different pressures. Clarke's model, based on the Debye approximation, assumes that the phonon mean free path is equal to the interatomic spacing and can be expressed as

$$k_{min} = 0.87 k_B M_a^{-\frac{2}{3}} E^{\frac{1}{2}} \rho^{\frac{1}{6}}, \tag{8}$$

$$M_a = \frac{M}{mN_A}, \tag{9}$$

where k_B is Boltzmann's constant, M_a is the average mass per atom in the unit cell, ρ represents density, M is the molar mass, m refers to the total number of atoms per unit cell, and N_A is Avogadro's number. Meanwhile, Cahill's model is mainly based on Einstein's model, and it can be expressed as

$$k_{min} = \frac{k_B}{2.48} n^{\frac{2}{3}} (v_l + 2v_t), \tag{10}$$

where n is the density of the number of atoms per unit volume. Unlike the Debye model, which assumes a continuous phonon spectrum, the Einstein model approximates phonons as independent oscillators with a characteristic frequency. Building upon this assumption, Cahill's model provides an estimate for the lower bound of thermal conductivity.

The calculated minimum thermal conductivities (k_{min}) of $oC10$-Mn_2AlB_2 and $tP10$-Mn_2AlB_2 at various pressures are summarized in Table 5. At 0 GPa, the k_{min} values of the $oC10$-Mn_2AlB_2 phase obtained by the two models are in good agreement with previously reported theoretical data.[18] However, because Clarke's model neglects the contribution of optical phonon modes to thermal conductivity, its calculated val-

ues are consistently slightly lower than those derived from Cahill's model. With increasing pressure, the k_{min} values for both $oC10$-Mn_2AlB_2 and $tP10$-Mn_2AlB_2 phases gradually increase, indicating enhanced phonon transport under compression. This trend correlates with the simultaneous increase in the Grüneisen parameter γ, which reflects stronger lattice anharmonicity and shorter bond lengths caused by pressure-induced lattice contraction, collectively promoting phonon propagation. Despite this increase, the k_{min} values remain greater than 1.25 $W{\cdot}m^{-1}{\cdot}K^{-1}$, suggesting that these phases are unlikely to function as highly efficient thermal barrier materials. Nevertheless, the observed tunability of k_{min} with pressure, together with the associated variation in γ, provides valuable insight into the thermal transport behavior of Mn_2AlB_2 and offers guidance for potential optimization strategies, such as defect engineering, alloying, or microstructural modulation, for high-temperature or heat-management applications.

Table 5. Calculated minimum thermal conductivities k_{min} ($W{\cdot}m^{-1}{\cdot}K^{-1}$) of different Mn_2AlB_2 phases at different pressures.

Space group	Pressure (GPa)	Clarke model		Cahill model		Ref.
		M_a (10^{-26})	k_{min}	N (10^{28})	k_{min}	
$oC10$	0	5.263	2.37	10.999	2.56	This work
	0		2.258		2.456	Cal.[18]
	10	5.263	2.48	11.474	2.71	This work
	21.5	5.263	2.66	11.933	2.91	This work
$tP10$	21.5	5.263	2.65	12.127	2.90	This work
	30	5.263	2.76	12.414	3.03	This work
	40	5.263	2.89	12.734	3.17	This work
	50	5.263	3.01	13.026	3.31	This work
	60	5.263	3.12	13.303	3.43	This work
	70	5.263	3.22	13.566	3.54	This work
	80	5.263	3.32	13.818	3.65	This work

3.4. Electronic properties and chemical bonding

To elucidate the electronic features and magnetic origins of Mn_2AlB_2 in different structures, we computed the spin-polarized total and projected density of states (DOS/PDOS) for the $oC10$ and $tP10$ phases, as depicted in Fig. 6. The vertical dashed line represents the Fermi level (E_F). Both phases exhibit metallic behavior with no band gap near the E_F. However, their distinct spin-resolved DOS profiles reveal a clear structure-dependent magnetic response. For the $oC10$ phase (Figs. 6(a) and 6(b)), the states near the Fermi level are dominated by Mn-d orbitals, and the pronounced asymmetry between the spin-up and spin-down channels indicates strong spontaneous magnetization. The Mn-d split peaks appear in the range of -2 eV to 2 eV, and their relatively narrow shapes suggest a partially localized character, which serves as the primary source of the magnetic moment. Meanwhile, strong Mn–B hybridization is observed from -6 eV to -2 eV, where the B-p and Mn-d states overlap and form directional Mn–B covalent bonds that enhance the structural stability of $oC10$-Mn_2AlB_2. This is consistent with previous findings.[18]

Upon transitioning to the $tP10$-Mn_2AlB_2 phase (Figs. 6(c) and 6(d)), the Mn-d DOS near the Fermi level undergoes notable changes: several d-orbital peaks become sharper, indicating enhanced localization. This is consistent with the transient increase in magnetic moment during the phase transition. Additionally, the redistribution and strengthening of B-p and Mn-d hybridization reshape the bonding environment and magnetic contributions, reflecting the electronic reconstruction associated with the structural change. With increasing pressure, the Mn-d bandwidth gradually broadens, and the exchange splitting near the Fermi level diminishes, resulting in a monotonic pressure-induced suppression of the magnetic moment.

Although the B/G ratio and Poisson's ratio are commonly employed as empirical indicators for distinguishing between brittle and ductile behavior, the numerical threshold of 1.75 should not be regarded as a strict physical boundary. To further validate the predictions based on elastic moduli, we analyzed the bonding characteristics using COHP analysis. The COHP profiles depicting the Mn–B, Mn–Al, Al–B, and B–B bonding interactions in $oC10$-Mn_2AlB_2 and $tP10$-Mn_2AlB_2 are presented in Fig. 7. As shown in Figs. 7(a) and 7(b), the COHP analysis reveals that the $oC10$ phase at low pressure is dominated by strong directional B–B covalent bonds, which restrict shear deformation and are typically associated with brittle behavior.

Table 6. Calculated negative integrated COHP (–ICOHP) values and bond distances of different Mn_2AlB_2 phases at different pressures.

Space group	Pressure (GPa)	Bonds	Bond distance (Å)	–ICOHP (eV/bond)
$oC10$	0	B–B	1.746	2.951
		Al–B	2.284	1.526
		Mn–Al	2.590	0.544
		Mn–B	2.132	0.866
	21.5	B–B	1.712	3.032
		Al–B	2.203	1.626
		Mn–Al	2.497	0.604
		Mn–B	2.088	0.923
$tP10$	21.5	B–B	3.110	0.054
		Al–B	2.199	1.623
		Mn–Al	2.449	0.528
		Mn–B	2.112	0.891
	80	B–B	2.973	0.061
		Al–B	2.102	1.710
		Mn–Al	2.343	0.586
		Mn–B	2.032	1.117

The negative integrated crystal orbital Hamilton populations (–ICOHPs) for both the $oC10$ and $tP10$ phases are summarized in Table 6. In $oC10$-Mn_2AlB_2, the -ICOHP values for B–B, Al–B, Mn–Al, and Mn–B bonds all increase with pressure, suggesting a progressive strengthening of the primary bonding interactions under compression. Among these, the B–B bonds exhibit the largest –ICOHP values, confirming that

B–B interactions are significantly stronger than the other bond types. Meanwhile, the antibonding states near the Fermi level remain weak, indicating that pressure reinforces the structure primarily by enhancing the occupation of bonding states rather than populating antibonding states. This trend aligns with the evolution of the elastic moduli: the bulk modulus B, the shear modulus G, and the ratio B/G all increase with pressure, reflecting an enhanced overall resistance to deformation.

Following the phase transition to the $tP10$-Mn_2AlB_2 phase, the bonding characteristics change markedly, as shown in Fig. 7(c). Mn–B and Al–B bonds become the dominant contributors to bonding, while the B–B contribution near the Fermi level is substantially diminished, indicating a shift in the primary bonding channels induced by structural reorganization. Upon further compression to 80 GPa (Fig. 7(d)), the COHP magnitudes of the Mn–B and Al–B bonds continue to rise, consistent with the –ICOHP values in Table 6. In the $tP10$-Mn_2AlB_2 phase, strong covalent B–B bonding weakens, and the dominant interactions are replaced by Mn–B and Al–B bonds. This means that the pressure mainly strengthens the collective metallic–covalent hybrid bonding, rather than the strong B–B covalency typically found in transition-metal borides.[46,49] The COHP results for $tP10$-Mn_2AlB_2 show that the main bonding interactions are uniformly enhanced with increasing pressure. Correspondingly, the B/G ratio and Poisson's ratio rise, indicating a relative reduction in shear rigidity and an improvement in ductility. Thus, the $tP10$-Mn_2AlB_2 phase exhibits reduced brittleness and enhanced toughness under high pressure, progressively developing mechanical behavior characterized by ductile dominance.

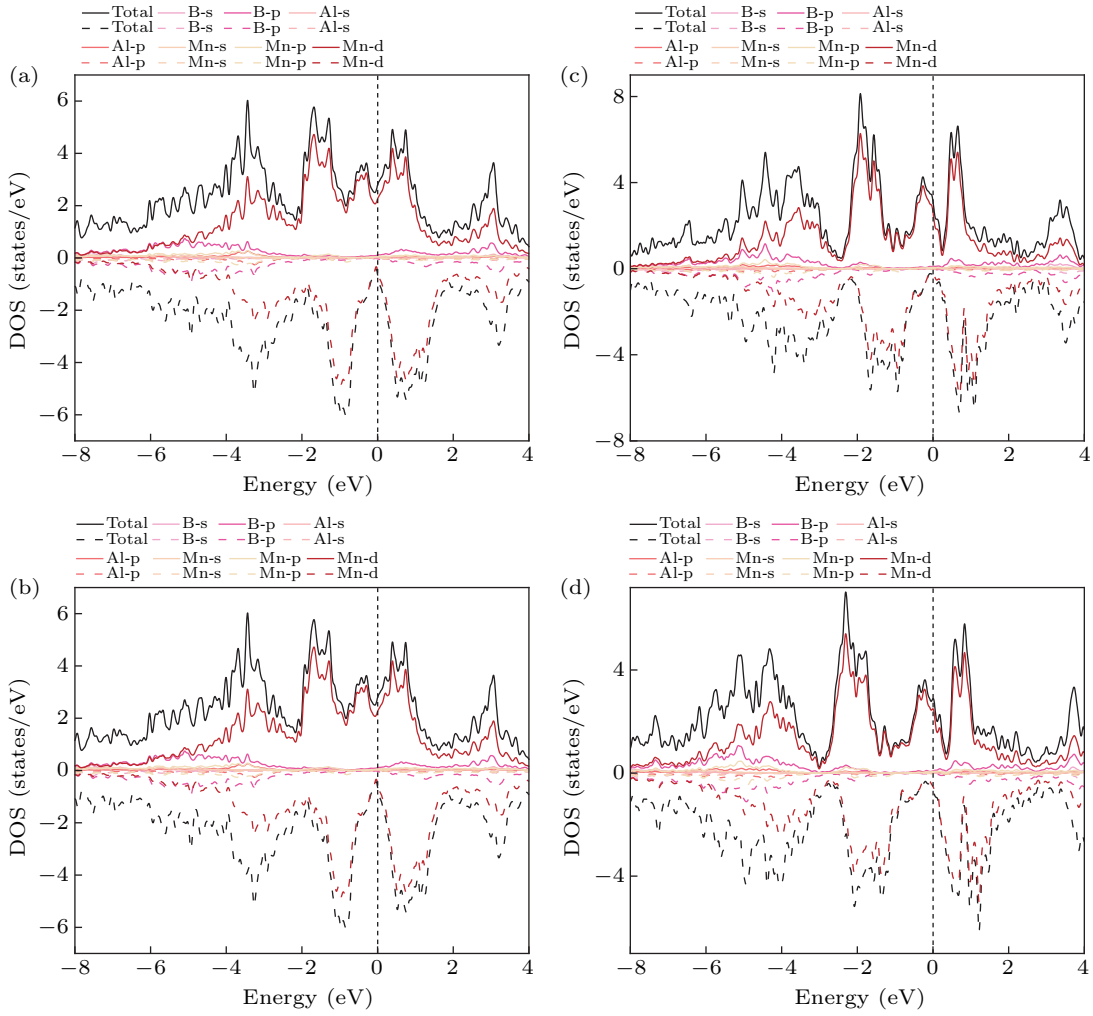


Fig. 6. Spin-polarized total and partial DOS of $oC10$-Mn_2AlB_2 at (a) 0 GPa and (b) 21.5 GPa, and $tP10$-Mn_2AlB_2 at (c) 21.5 GPa and (d) 80 GPa. Solid lines denote spin-up states, and dashed lines denote spin-down states. The vertical dashed line at zero indicates the Fermi energy level.

To understand electron pairing and localization in $oC10$-Mn_2AlB_2 and $tP10$-Mn_2AlB_2, we further computed the electron localization function (ELF),[57] which can be seen in Fig. 8. An ELF value of one corresponds to perfect electron localization, indicative of covalent bonding; a value of 0.5 reflects a homogeneous electron-gas distribution; and ELF = 0 represents complete delocalization. In the $oC10$-Mn_2AlB_2 phase (Figs. 8(a) and 8(b)), pronounced high-ELF regions (red–orange, ELF ≈ 0.6–0.8) are observed between B atoms, signifying strong covalent B–B interactions that form a directional bonding framework. With increasing pressure, these high-ELF regions become more intense and continu-

ous, demonstrating pressure-enhanced B–B bonding, consistent with the strengthening trend observed in the COHP analysis. In contrast, the Mn–B and Al–B regions exhibit intermediate ELF values (green–yellow, ELF ≈ 0.3–0.5), characteristic of mixed metallic–covalent interactions. Under compression, these intermediate regions strengthen moderately but do not show pronounced directional enhancement, suggesting that Mn–B and Al–B bonds are reinforced in a relatively uniform manner.

After the transition to the $tP10$-Mn_2AlB_2 phase (Figs. 8(c) and 8(d)), the ELF distribution changes markedly. While B–B localization remains high, the Mn–B and Al–B ELF isosurfaces become more uniform, indicating a more homogeneous electron distribution throughout the structure. With increasing pressure, strong B–B localization persists, consistent with its significantly lower –ICOHP values compared to those of Mn–B and Al–B in the COHP results. Meanwhile, the ELF around Mn–B and Al–B becomes smoother and lacks strong directional enhancement, showing that pressure primarily strengthens the overall bonding network rather than promoting specific localized bonds. These observations explain why the $tP10$-Mn_2AlB_2 phase exhibits reduced brittleness and enhanced ductility under pressure, ultimately evolving toward mechanical behavior dominated by ductile characteristics.

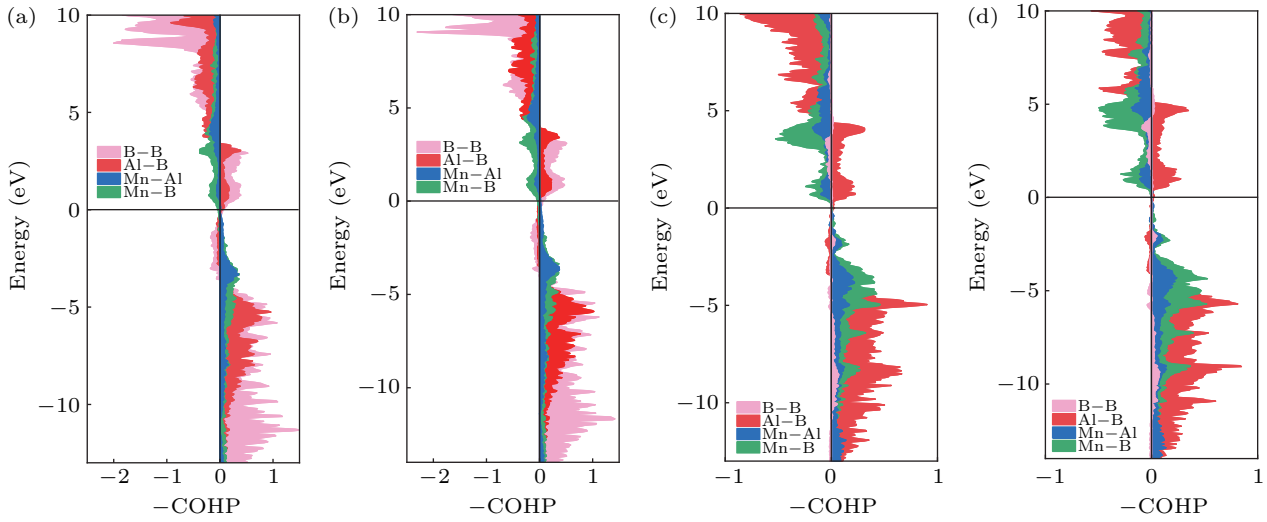


Fig. 7. Negative COHP curves for $oC10$-Mn_2AlB_2 at (a) 0 GPa and (b) 21.5 GPa, and $tP10$-Mn_2AlB_2 at (c) 21.5 GPa and (d) 80 GPa. Here, a positive value represents a bonding interaction, and a negative value represents an antibonding state.

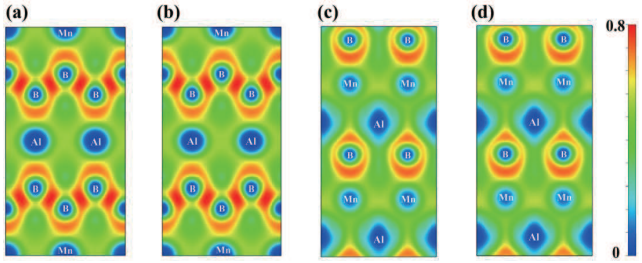


Fig. 8. Calculated electron localization function (ELF) maps for $oC10$-Mn_2AlB_2 at (a) 0 GPa and (b) 21.5 GPa on the (100) plane, and $tP10$-Mn_2AlB_2 at (c) 21.5 GPa and (d) 80 GPa on the (100) plane.

To further clarify the pressure-induced magnetic evolution of Mn_2AlB_2, we calculated the local magnetic moments of Mn at different pressures, as listed in Table 7. The results reveal that in the $oC10$-Mn_2AlB_2 phase, the Mn magnetic moment decreases from 0.503 μ_B·atom^{-1} at 0 GPa to 0.336 μ_B·atom^{-1} at 21.5 GPa. Similarly, in the $tP10$-Mn_2AlB_2 phase, it declines from 0.528 μ_B·atom^{-1} at 21.5 GPa to 0.477 μ_B·atom^{-1} at 80 GPa. This consistent reduction indicates that pressure effectively suppresses Mn spin polarization and weakens the FM order. This magnetic evolution aligns with changes in the electronic structure and bonding behavior. With increasing pressure, the Mn-3d bands in the PDOS broaden, leading to reduced spin splitting. Concurrently, COHP analysis shows enhanced Mn–B and Mn–Al bonding interactions, while ELF results indicate decreased electron localization. These features collectively demonstrate that pressure promotes stronger bonding and greater electronic delocalization, which themselves act to suppress the local magnetic moments and weaken the overall magnetism of Mn_2AlB_2.

Table 7. Calculated local magnetic moments of Mn in different Mn_2AlB_2 phases under different pressures.

Space group	Pressure (GPa)	Magnetic moment (μ_B/Mn)
$oC10$	0	0.503
	0	0.430[18]
	10	0.412
	21.5	0.336
$tP10$	21.5	0.528
	30	0.512
	40	0.502
	50	0.497
	60	0.492
	70	0.486
	80	0.477

3.5. Pressure–temperature phase diagram

In the previous section, the pressure-induced phase transition order ($oC10$-$Mn_2AlB_2 \rightarrow tP10$-$Mn_2AlB_2$) was determined at 0 K. Phonon frequency calculations confirm that both phases are dynamically stable over a wide pressure range. Using the quasi-harmonic approximation (QHA),[58] the pressure–temperature phase diagram was further investigated at elevated pressures and temperatures. In the QHA framework, the Helmholtz free energy at a given pressure and temperature is expressed as follows:

$$F(V,T) = E(V) + F_{\text{vib}}(V,T), \tag{11}$$

where the static energy $E(V)$ is the total energy, and $F_{\text{vib}}(V,T)$ is the nonequilibrium vibrational Helmholtz free energy obtained from

$$F_{\text{vib}}(V,T) = \int_0^{\infty} \left[\frac{\hbar\omega}{2} + \kappa_B T \ln\left(1 - e^{\frac{-\hbar\omega}{\kappa_B T}}\right)\right] g(\omega,V)\,\mathrm{d}\omega, \tag{12}$$

where $g(\omega,V)$ is the phonon density of states and depends on the crystal geometry. Then, the Gibbs free energy G_{gibbs} is as follows:

$$G_{\text{gibbs}} = F(V,T) - V\left(\frac{\partial F}{\partial V}\right)_T. \tag{13}$$

In this work, 11 sets of volume, energy, and phonon density of states data were selected for data fitting of both the $oC10$-Mn_2AlB_2 and $tP10$-Mn_2AlB_2 phases. Based on the calculated results, a pressure–temperature phase diagram of Mn_2AlB_2 under high-pressure and finite temperature conditions was created for the first time (see Fig. 9). As shown in the figure, the effect of temperature is evident: with increasing temperature, the transition pressure gradually decreases. At room temperature (300 K), the phase transition occurs at approximately 18 GPa.

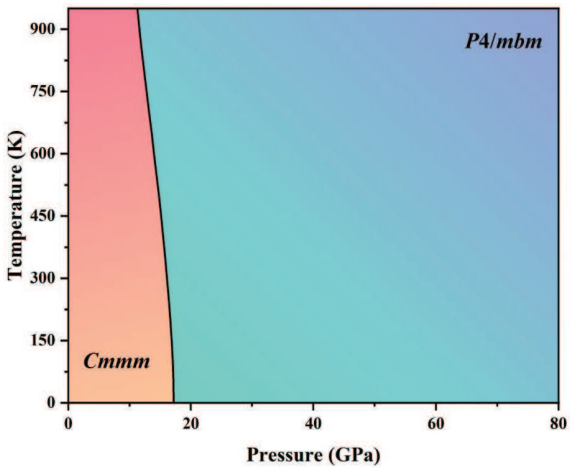


Fig. 9. Phase diagram of Mn_2AlB_2 at high pressure and finite temperature.

4. Conclusion

The pressure-induced phase transition of Mn_2AlB_2 was investigated using the PSO algorithm. The results indicate that $oC10$-Mn_2AlB_2 transforms into $tP10$-Mn_2AlB_2 at approximately 21.5 GPa, accompanied by a 1.6% volume reduction, confirming a first-order phase transition. First-principles calculations of the elastic constants and phonon dispersion relations demonstrate that both phases are mechanically and dynamically stable throughout the investigated pressure range. Analysis of the B/G ratio indicates that $oC10$-Mn_2AlB_2 is brittle from 0 to 21.5 GPa, while $tP10$-Mn_2AlB_2 exhibits brittleness at 21.5–40 GPa and ductility at 40–80 GPa, indicating that pressure can effectively tune the material's brittleness and ductility. The Vickers hardness results further suggest that both phases are hard materials, with hardness increasing under pressure. Furthermore, the minimum thermal conductivity of both phases exceeds 1.25 $W{\cdot}m^{-1}{\cdot}K^{-1}$ and increases slightly with pressure, indicating limited thermal insulation capability. Analysis of the electronic structure and bonding in the two Mn_2AlB_2 phases clearly shows that pressure strengthens the Mn–B and Al–B bonding interactions, leading to enhanced electronic delocalization and reduced magnetic moments. Finally, a high-pressure and high-temperature phase diagram constructed using the QHA shows that the transition pressure from $oC10$-Mn_2AlB_2 to $tP10$-Mn_2AlB_2 decreases with increasing temperature.

Acknowledgments

Project supported by the National Natural Science Foundation of China (Grant Nos. 12404063 and 11904282), the Foundation of the National Key Laboratory of Computational Physics (Grant No. SYSQN2024-01), and the Natural Science Basic Research Program of Shaanxi Province (Grant Nos. 2024JC-YBQN-0044 and 2023-JC-QN-0068).

References

[1] Lei X and Lin N 2022 *Crit. Rev. Solid State Mater. Sci.* **47** 736
[2] Gonzalez Julian J 2021 *J. Am. Ceram. Soc.* **104** 659
[3] Sun Z M 2011 *Int. Mater. Rev.* **56** 143
[4] Eklund P, Beckers M, Jansson U, Högberg H and Hultman L 2010 *Thin Solid Films* **518** 1851
[5] Kádas K, Iuşan D, Hellsvik J, Cedervall J, Berastegui P, Sahlberg M, Jansson U and Eriksson O 2017 *J. Phys. Condens. Matter* **29** 155402
[6] Barsoum M W and El Raghy T 1996 *J. Am. Ceram. Soc.* **79** 1953
[7] Yoo H I, Barsoum M and El Raghy T 2000 *Nature* **407** 581
[8] Joksas D, AlMutairi A, Lee O, Cubukcu M, Lombardo A, Kurebayashi H, Kenyon A J and Mehonic A 2022 *Adv. Intell. Syst.* **4** 2200068
[9] Fu L and Xia W 2021 *Adv. Eng. Mater.* **23** 2001191
[10] Liu Y Y, Wang Y X, Yan Z X, Liu W, Zhou G L, Xiong K Z and Gu J B 2022 *Philos. Mag.* **102** 228
[11] Kota S, Sokol M and Barsoum M W 2020 *Int. Mater. Rev.* **65** 226
[12] Bai Y, Sun D, Li N, Kong F, Qi X, He X, Wang R and Zheng Y 2019 *Int. J. Refract. Met. Hard Mater.* **80** 151
[13] Roy C, Mondal S, Banerjee P and Bhattacharyya S 2023 *Adv. Powder Technol.* **34** 103983

[14] Qin K, Qi X, Gao J, He X, Yin H, Yin W, Song G, Zheng Y and Bai Y 2024 *J. Am. Ceram. Soc.* **107** 5313
[15] Ade M and Hillebrecht H 2015 *Inorg. Chem.* **54** 6122
[16] Kota S, Chen Y, Wang J, May S J, Radovic M and Barsoum M W 2018 *J. Eur. Ceram. Soc.* **38** 5333
[17] Potashnikov D, Caspi E, Pesach A, Hoser A, Kota S, Verger L, Barsoum M, Felner I, Keren A and Rivin O 2019 *J. Magn. Magn. Mater.* **471** 468
[18] Surucu G, Yildiz B, Erkisi A, Wang X and Surucu O 2020 *J. Alloys Compd.* **838** 155436
[19] Liu Y, Sun L, Zheng B, Yi Y, Zhai W, Peng J and Li W 2021 *Ceram. Int.* **47** 1421
[20] Kota S, Agne M T, Imasato K, El Melegy T A, Wang J, Opagiste C, Chen Y, Radovic M, Snyder G J and Barsoum M W 2022 *J. Eur. Ceram. Soc.* **42** 3183
[21] Wang Y, Lv J, Zhu L and Ma Y 2010 *Phys. Rev. B.* **82** 094116
[22] Wang Y, Lv J, Zhu L and Ma Y 2012 *Comput. Phys. Commun.* **183** 2063
[23] Wang Q, Wei J, Zhong T, Sun J, Gao B, Zhu L, Liu H and Zhang S 2024 *Phys. Rev. B* **110** 144523
[24] Yan Q, Zhang X, Chen J, Tang Y, Ni Y, Wang H, Liu Z and Chen Y 2024 *J. Phys. Chem. C* **128** 21551
[25] Wu H, Wang Y X, Yan Z X, Liu W, Wang Z Q and Gu J B 2023 *Appl. Phys. A* **129** 175
[26] Kresse G and Furthmüller J 1996 *Phys. Rev. B* **54** 11169
[27] Kresse G and Furthmüller J 1996 *Comput. Mater. Sci.* **6** 15
[28] Wang V, Xu N, Liu J C, Tang G and Geng W T 2021 *Comput. Phys. Commun.* **267** 108033
[29] Kresse G and Joubert D 1999 *Phys. Rev. B* **59** 1758
[30] Perdew J P, Burke K and Ernzerhof M 1996 *Phys. Rev. Lett.* **77** 3865
[31] Voigt W 1928 *Adv. Earth Sci.* **1** 1
[32] Reuß A 1929 *ZAMM-Journal Appl. Math. Mech. Für Angew. Math. Mech.* **9** 49
[33] Hill R 1952 *Proc. Phys. Soc. Sect. A* **65** 349
[34] Wu Z, Zhao E, Xiang H, Hao X, Liu X and Meng J 2007 *Phys. Rev. B.* **76** 054115
[35] Togo A, Oba F and Tanaka I 2008 *Phys. Rev. B.* **78** 134106
[36] Togo A and Tanaka I 2015 *Scr. Mater.* **108** 1
[37] Anisimov V I, Solovyev I, Korotin M, Czyżyk M and Sawatzky G 1993 *Phys. Rev. B* **48** 16929
[38] Dronskowski R and Bloechl P E 1993 *J. Phys. Chem.* **97** 8617
[39] Steinberg S and Dronskowski R 2018 *Crystals* **8** 225
[40] Dal Corso A 2016 *J. Phys. Condens. Matter* **28** 075401
[41] Mouhat F and Coudert F X 2014 *Phys. Rev. B* **90** 224104
[42] Pugh S 1954 *Lond. Edinb. Dublin Philos. Mag. J. Sci.* **45** 823
[43] Haines J, Leger J and Bocquillon G 2001 *Annu. Rev. Mater. Res.* **31** 1
[44] Bouhemadou A, Allali D, Bin Omran S, Al Safi E M A, Khenata R and Al Douri Y 2015 *Mater. Sci. Semicond. Process.* **38** 192
[45] Chen X Q, Niu H, Li D and Li Y 2011 *Intermetallics* **19** 1275
[46] Liang Y, Gou Y, Yuan X, Zhong Z and Zhang W 2013 *Chem. Phys. Lett.* **580** 48
[47] Misra A and Ching W Y 2013 *Sci. Rep.* **3** 1488
[48] Chen X Q, Niu H, Franchini C, Li D and Li Y 2011 *Phys. Rev. B.* **84** 121405
[49] Wang X F, Wang Y X, Wang Z, Zhang Y X and Gu J B 2024 *Chin. Phys. B* **33** 126103
[50] Huang B, Duan Y H, Hu W C, Sun Y and Chen S 2015 *Ceram. Int.* **41** 6831
[51] Anderson O L 1963 *J. Phys. Chem. Solids* **24** 909
[52] Shen Y, Clarke D R and Fuierer P A 2008 *Appl. Phys. Lett.* **93** 102907
[53] Feng J, Xiao B, Zhou R, Pan W and Clarke D R 2012 *Acta Mater.* **60** 3380
[54] Clarke D R 2003 *Surf. Coat. Technol.* **163** 67
[55] Clarke D and Levi C 2003 *Annu. Rev. Mater. Res.* **33** 383
[56] Cahill D G, Watson S K and Pohl R O 1992 *Phys. Rev. B* **46** 6131
[57] Morales Bayuelo A and Sánchez Márquez J 2020 *Heliyon* **6** e04441
[58] Otero De La Roza A, Abbasi Pérez D and Luaña V 2011 *Comput. Phys. Commun.* **182** 2232